N O T I C E

THIS DOCUMENT HAS BEEN REPRODUCED FROM
MICROFICHE. ALTHOUGH IT IS RECOGNIZED THAT
CERTAIN PORTIONS ARE ILLEGIBLE, IT IS BEING RELEASED
IN THE INTEREST OF MAKING AVAILABLE AS MUCH
INFORMATION AS POSSIBLE

72N 19996

NASA TECHNICAL MEMORANDUM

NASA TM-76676

EXPERIMENTAL INVESTIGATION OF A TRANSSONIC POTENTIAL
FLOW AROUND A SYMMETRIC AIRFOIL

W.J. Hiller, G.E.A. Meier

Translation of
"Experimentelle Untersuchung einer transsonischen Potentialströmung
um ein symmetrisches Tragflügelprofil", Max-Planck Institut Für
Strömungsforschung, Göttingen, W. Germany, Report 10/1971, Nov
1971, 22 pages.

NATIONAL AERONAUTICS AND SPACE ADMINISTRATION
WASHINGTON, DC 20546   DECEMBER 1981

1. Report No. NASA TM-76676	2. Government Accession No.	3. Recipient's Catalog No.
4. Title and Subtitle EXPERIMENTAL INVESTIGATION OF A TRANSSONIC POTENTIAL FLOW AROUND A SYMMETRIC AIRFOIL		5. Report Date December 1981
		6. Performing Organization Code
7. Author(s) W.J. Hiller and G.E.A. Meier		8. Performing Organization Report No.
		10. Work Unit No.
9. Performing Organization Name and Address Leo Kanner Associates Redwood City, CA 94063		11. Contract or Grant No. NASW-3541
		13. Type of Report and Period Covered
12. Sponsoring Agency Name and Address National Aeronautics and Space Administration, Washington, D.C. 20546		translation
		14. Sponsoring Agency Code

15. Supplementary Notes

Translation of "Experimentelle Untersuchung einer transsonischen Potentialströmung un ein symmetrisches Tragflügelprofil," Max-Planck Institut für Strömungsforschung, Göttingen, W. Germany, Report 10/1971, Nov. 1971, 22 pages.

(German: N72-19996)

16. Abstract
Experimental flow investigations on smooth airfoils were done using numerical solutions for transsonic airfoil streaming with shockless supersonic range. The experimental flow reproduced essential sections of the theoretically computed frictionless solution. Agreement is better in the expansion part of the flow than in the compression part. The flow was nearly stationary in the entire velocity range investigated.

17. Key Words (Selected by Author(s))	18. Distribution Statement Unclassified – Unlimited

19. Security Classif. (of this report) Unclassified	20. Security Classif. (of this page) Unclassified	21. No. of Pages 23	22.

CONTENTS

1. The Studied Airfoil

The starting point for our experimental flow investigations on smooth airfoils was the numeric solutions for transsonic airfoil streaming with shockless supersonic range computed by G.Y. Nieuwland [1] and J.W. Boerstoel [2] using the method of T.M. Cherry and M.J. Lighthill. Through these tests we shall determine whether this shockless compression is a physical possibility.

The original symmetric airfoil provided for the experiments 0.1100 - 0.7500 - 1.3750 (fig. 1) was replaced after consultation with J.W. Boerstoel of the NLR (National Lucht-en Ruimtevaart Laboratorium, Amsterdam), by the profile 0.10 - 0.676 - 1.6 (fig. 2), because the latter is supposed to have less tendency for parting of the laminar boundary layer at the airfoil nose and should give greater supersonic speeds at smaller Mach number of incident flow. This airfoil is still symmetric, it is 16.3% thick and is designed for an incident Mach number $Ma = 0.745$ with an incident-flow angle $\alpha = 0^o$. The greatest Mach number in the supersonic range--which is assumed to be far in front of the thickest point of the airfoil--amounts to $Ma = 1.464$. The profile coordinates, whose computation is very complex, were provided to us by the NLR.

By using these coordinates, a profile template of ca. 635 mm length of chord was produced whose deviation from the theoretical value is less than 0.05 mm. This accuracy of application was easily achieved with the coordinatographs available to us. Using this template, a 5-fold smaller test model was produced by means of a duplicating milling machine. For a tight fit of spindles and joints in the machine, an accuracy of 0.01 mm can be attained in this manner.

2. Test Equipment

The profile (fig. 3) is anchored with two each laterally

attached retaining pins in appropriate drilled holes of the 35 mm
thick canal window (fig. 4). This type of attachment prevents
additional disturbances of the flow due to holding devices pro-
truding into the canal. In addition, with this set-up, the
set angle of the profile can be easily adjusted from the outside
and measured. The depth of the profile is 100 mm (corresponding
to canal depth), the length 126.8 mm and the max. thickness 20.68
mm. The canal height is limited to 300 mm (fig. 5) by two canal
walls slit in the flow direction; these walls can also be deformed,
depending on their location (fig. 6). Thus, the flow generated in
the canal can be adapted to the free profile streaming [3]. The
opened canal rotated about a horizontal axis by 90° clearly shows
the half of the comb-like setting-diffusor, with which the through-
put is regulated. Figure 8 shows a complete picture of the test
arrangement. The pipeline entering the picture on the upper right
connects the test canal to the vacuum vessel via a fast-acting
valve. Under the canal is a Mach-Zehnder Interferometer with
attached high-frequency flash-lamp, to the left of this, the per-
tinent power supply unit. Behind the Mach-Zehnder Interferometer
we see a part of the differential interferometer. Both optic
instruments are movable on rails and can be used optionally to
view the streaming.

The canal (wind tunnel) is operated intermittently with
atmospheric air which flows into an evacuated vessel of 134 m^3
after passing through the measurement lane. Feed to the canal
with dry air was not possible for the tests described here since
the pipeline from the existing air drier to the canal is not
properly sized for these experiments and thus an excessive pressure
drop would result. At present, a gasometer of ca. 40 m^3 volume
is under development which will allow any adjustment of air humid-
ity to permit a study of the influence of this parameter.

For the investigation of flow with the Mach-Zehnder Interfero-
meter, the instrument was adjusted for infinite strip width under
a calm flow medium. In this case the interference strips correspond

2

to lines of constant density, if the deviations of the flow from the planar case can be neglected (e.g. wall boundary layer at the canal side-walls, secondary streaming). An estimation of the boundary layer thickness at the canal walls in the measured range (ignoring the influence of the airfoil) gives a maximum value of 0.02 mm.

To register the interference pictures, a mirror-reflex camera and a high-speed camera (picture frequency up to 10 kHz) are used. A stroboscope is used as light source. The duration of the individual flashes is ca. 1 us, the converted electrical energy ca. 1 Joule.

3.   Study Results

In general, we can say that the experimental flow reproduces essential sections of the theoretically computed frictionless solution. In the expansion part of the flow, the agreement is clearly better than in the compression part, since there the boundary layer increases quickly and its compression action changes the velocity field. The boundary layer is seen in the interferograms by the sudden bending of interference lines near the airfoil (e.g. fig. 9). It should be mentioned that the flow—except for the turbulent wake and the sound disruptions generated there—is nearly stationary in the entire velocity range investigated by us. One important prerequisite for this behavior lies in the large stability of the turbulent boundary layer in the range $0.2 < \frac{x}{l} \leqslant 1$ against flow becoming non-laminar, even in the presence of compression shocks (e.g. fig. 13).

The typical run of the experimentally found flow state is presented in the interference pictures 9 - 13. The subsequent, dashed line gives the position of the theoretically calculated sound barrier for an incident flow Mach number $M_{oo} = 0.745$. In our tests (rest pressure p_o = 745 mm Qs, rest temperature 20 $^\circ$C, depth of canal b = 100 mm, wavelength of used light λ = 567 nm),

3

the sound barrier corresponds to interference strip with the order m = 17.25, if the order of the interference in the stagnation point of the airfoil is specified as m = 0 (see table). The Mach number of incident flow is determined from the interference pictures with an accuracy of 5%. In our previous investigations we found that in all cases in which a supersonic region appeared, a slanting compression shock goes out from the profile nose, which is reflected repeatedly between the sonic barrier and profile (under circumstances as an attenuation fan). The origin of the shock lies just behind the point of maximum curvature of the profile nose (fig. 14). Since in the interference pictures the suspected non-laminar flow as source for the occurrence of the compression shock cannot definitely be found, the flow was also examined by using the tinting method. For this purpose, the profile was subjected to a suspension of titanium dioxide in oil as spray, and then exposed ca. 5 s to the flow. The tests showed that behind the point of maximum curvature, there is formation of a dead-water region of ca. 5 mm length. In the tinting pictures (fig. 19, 20) we see the position of the non-laminar region and that there the sprayed-on suspension remains on the profile, whereas both in front and behind it, the suspension has been blown off almost completely by the flow. In addition, the pictures also show that the dead-water region does not extend up to the canal side walls, but ends ca. 10 mm in front of this. Apparently, the conversion of the laminal profile boundary layer occurs here, due to the effects of the turbulent wall boundary layer; it is earlier in this case so that the separation of flow of the wall boundary layer does not occur at these places.

As long as the observed supersonic range is larger or about equal to the calculated one, it is concluded by one or more weak, perpendicular, almost stationary compression shocks, whose origin we view as the flow field changed by the compression shock emanating from the profile nose. The disturbances emanating from the turbulent wake of the airfoil do not indicate any larger influence on the position and intensity of shocks (fig. 12, 13). If the super-

4

sonic range is smaller than the calculated one, then it breaks down into a sequence of weak shocks and expansion fans.

Another type of disturbance of the flow field is caused by the liberated heat on condensation of the water vapor contained in the atmospheric air. Figures 15-18 show the condensed water vapor in dark-field illumination. The relative humidity of the air was 50% as rest. The added heat can also be detected in the interference strips. Figures 15, 16 correspond to flow state of fig. 11, figures 17, 18, correspond to that of fig. 13.

Until now, no use had been made of the possibility mentioned above for adapting the canal contours (fig. 5, 6) to the flow lines expected in the free flow, since from other experiments it was supposed that the longitudinal slit in the canal walls would cause the majority of the compensation flow. A sample change had no effect on the shape of the compression shocks at the profile front edge, whereas the other flow field was changed only to a minor degree. The position-dependent setting of the contours thus only comes into consideration for fine-tuning the flow outside the near-field of the profile.

The pressure distributions calculated from the interferograms (fig. 9-15) along the profile are presented in figures 9a, b - 13a, b. Instead of the pressure coefficient c_p in fig. 2, we plotted the run of $\frac{p_0 - p}{p_0}$ (p_0 = stagnation pressure, p = static pressure) against the dimensionless length of chord $\frac{x}{l}$ since in our test set-up, the inflow velocity could not be determined very accurately from the interferograms. However, the coordinate system has an affinity with that of fig. 2. As long as the boundary layer is thin enough to be neglected, the pressure was determined from the order of interference at the particular profile location. As soon as the run of the interference strips indicates the shape of a boundary layer, the calculation of pressure takes place with the value of the interference order outside the boundary layer.

5

If we compare the obtained curves with those calculated from the theory, then we see a good qualitative agreement with regard to the profile. But on detailed consideration it turns out that due to the compression shock emanating from the "corner" of the profile nose, attainment of the expected underpressure peak is prevented and thus the structure of the computed flow field is disrupted. For $\frac{x}{l} > 0.2$, the theoretical pressure distribution is falsified by the quickly increasing compression effect of the boundary layer. Even now we can say with certainly that for the region $0.2 \leqslant \frac{x}{l} \leqslant 1$, the frictionless, calculated profile will have to be corrected by modification of the contour or suction-removal in order to attain the calculated pressure distribution.

REFERENCES

[1] G.Y. Nieuland: Transonic potential flow around a family of quasi-elliptical aerofoil sections. NLR TR T 172, 1967.

[2] J.W. Boerstoel: A survey of symmetrical transsonic potential flows around quasi-elliptical aerofoil sections. NLR TR T 136, 1967.

[3] Bernhard H. Goethert: Transonic Wind Tunnel Testing. AGARDograph 49, 1961.

7

Relation between interference strip arrangement. Density, pressure, temperature and Mach-number. (Prerequisites: Isotropic flow, rest pressure, p = 745 mm QS, rest temp. T = 20 °C, light wavelength λ = 567 nm, depth of tunnel b = 100 mm).

m	$\varrho : \varrho_0$	$p : p_0$	$T : T_0$	Ma	m	$\varrho : \varrho_0$	$p : p_0$	$T : T_0$	Ma
0.0	1.0	1.0	1.0	0.05	17.5	0.6289	0.521	0.828	1.01
0.5	0.989	0.985	0.996	0.15	18.0	0.6183	0.51	0.823	1.03
1.0	0.979	0.971	0.9916	0.208	18.5	0.6077	0.497	0.817	1.05
1.5	0.968	0.956	0.9875	0.25	19.0	0.5971	0.485	0.812	1.07
2.0	0.958	0.941	0.983	0.295	19.5	0.5865	0.473	0.806	1.09
2.5	0.947	0.925	0.977	0.333	20.0	0.5759	0.461	0.8	1.11
3.0	0.936	0.91	0.973	0.37	20.5	0.5653	0.45	0.794	1.13
3.5	0.926	0.896	0.969	0.398	21.0	0.5547	0.438	0.788	1.152
4.0	0.915	0.882	0.964	0.424	21.5	0.5441	0.426	0.782	1.174
4.5	0.905	0.87	0.9605	0.452	22.0	0.5335	0.416	0.777	1.196
5.0	0.894	0.855	0.956	0.48	22.5	0.5229	0.403	0.769	1.218
5.5	0.883	0.84	0.951	0.505	23.0	0.5123	0.39	0.763	1.242
6.0	0.873	0.826	0.946	0.53	23.5	0.5017	0.38	0.756	1.262
6.5	0.862	0.811	0.9418	0.555	24.0	0.4911	0.369	0.75	1.284
7.0	0.852	0.797	0.937	0.579	24.5	0.4805	0.358	0.744	1.305
7.5	0.841	0.783	0.932	0.6	25.0	0.4699	0.346	0.737	1.33
8.0	0.8304	0.771	0.927	0.62	25.5	0.4593	0.335	0.73	1.352
8.5	0.8198	0.755	0.9225	0.645	26.0	0.4487	0.325	0.723	1.377
9.0	0.8092	0.742	0.918	0.668	26.5	0.4381	0.314	0.717	1.4
9.5	0.7986	0.73	0.9139	0.686	27.0	0.4275	0.304	0.71	1.423
10.0	0.788	0.715	0.908	0.71	27.5	0.4169	0.293	0.7025	1.449
10.5	0.777	0.702	0.903	0.727	28.0	0.4063	0.282	0.694	1.475
11.0	0.7668	0.688	0.8975	0.75	28.5	0.3957	0.272	0.687	1.5
11.5	0.756	0.675	0.8925	0.77	29.0	0.3851	0.262	0.68	1.526
12.0	0.746	0.661	0.8875	0.79	29.5	0.3745	0.253	0.673	1.55
12.5	0.735	0.648	0.8825	0.81	30.0	0.3639	0.243	0.665	1.579
13.0	0.724	0.635	0.877	0.83	30.5	0.3533	0.232	0.657	1.61
13.5	0.714	0.623	0.8725	0.849	31.0	0.3427	0.222	0.648	1.64
14.0	0.703	0.61	0.867	0.87	31.5	0.3321	0.213	0.641	1.665
14.5	0.693	0.597	0.862	0.89	32.0	0.3215	0.203	0.632	1.696
15.0	0.682	0.583	0.857	0.91	32.5	0.3109	0.194	0.624	1.727
15.5	0.671	0.571	0.851	0.93	33.0	0.3003	0.185	0.615	1.76
16.0	0.661	0.56	0.846	0.948	33.5	0.2897	0.175	0.605	1.795
16.5	0.6502	0.547	0.84	0.97	34.0	0.2791	0.167	0.597	1.822
17.0	0.6396	0.532	0.835	0.991	34.5	0.2685	0.158	0.586	1.86
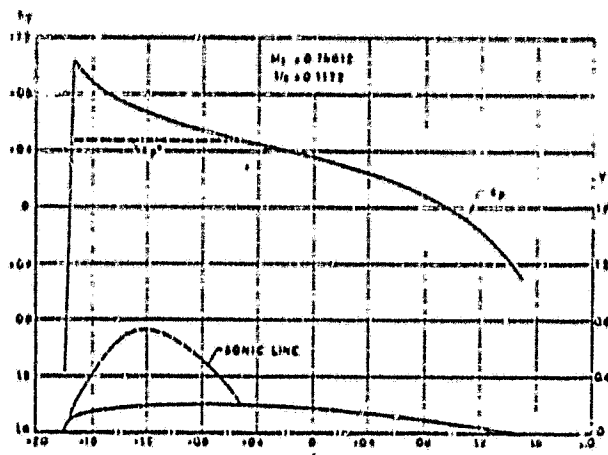
Figure 1: Pressure Coefficient and Shape of the Profile
0.11-0.75-1.375
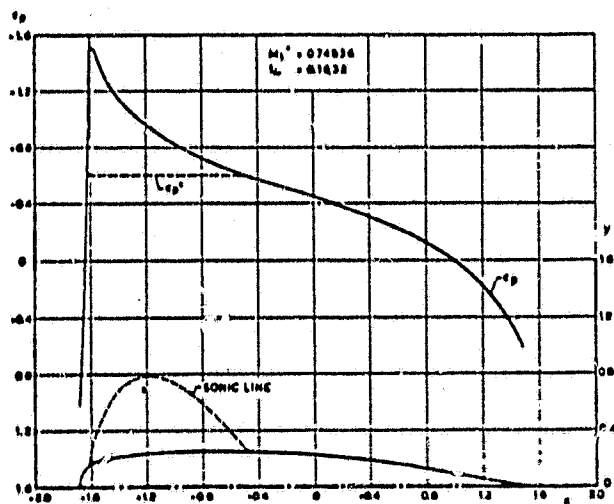
Figure 2: Pressure Coefficient and Shape of the Profile
0.10-0.675-1.6
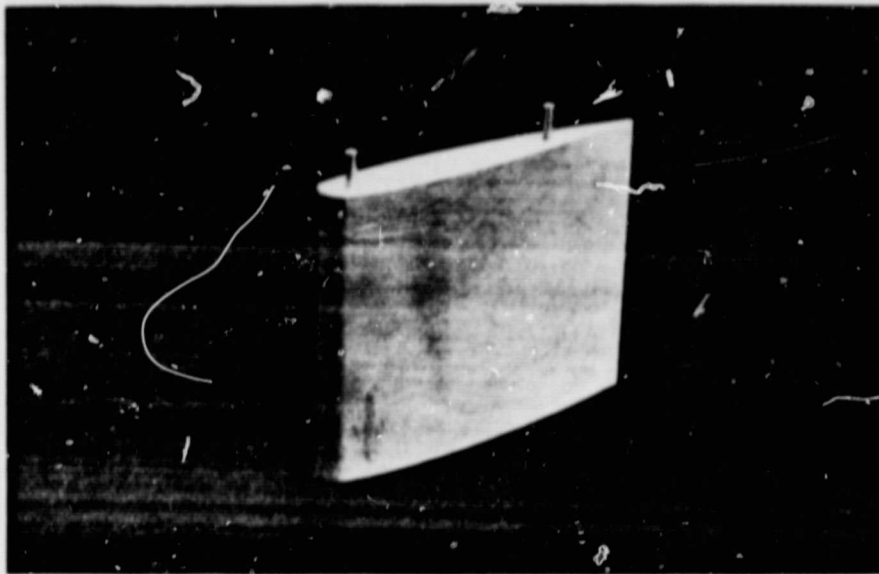
Figure 3: Airfoil Profile
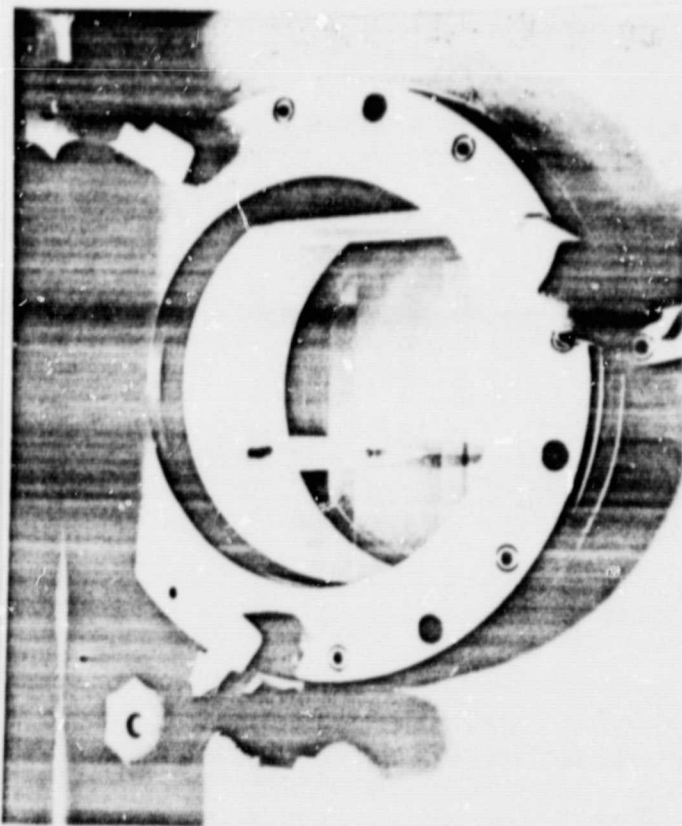
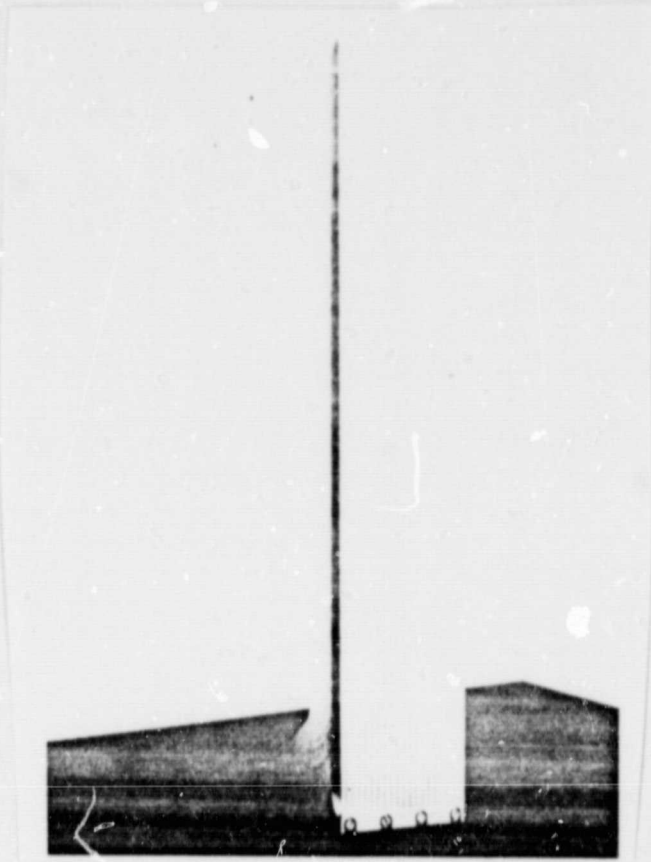Figure 4: Wind Tunnel Window with Installed Profile

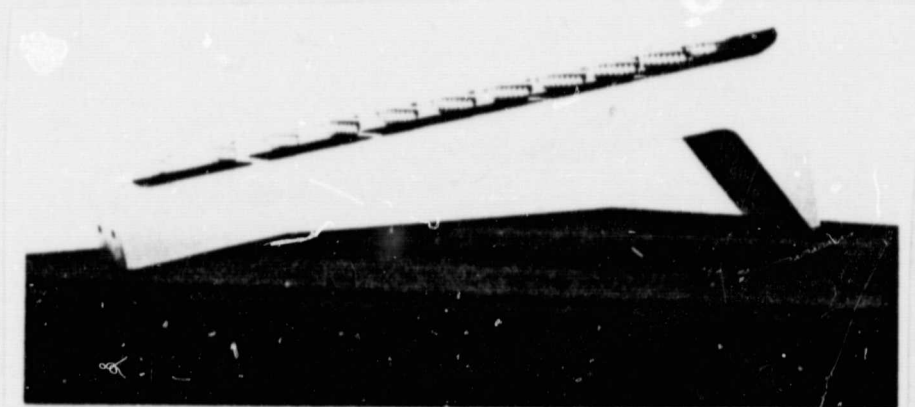10

Figure 5: Tunnel Wall (Slit in Flow Direction)

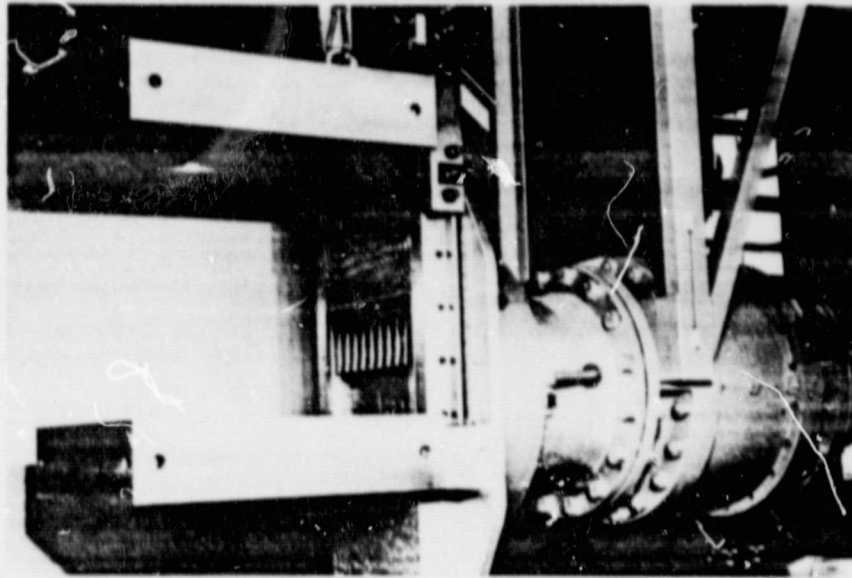Figure 6: Wind-tunnel Wall (Variable Wall Shape)

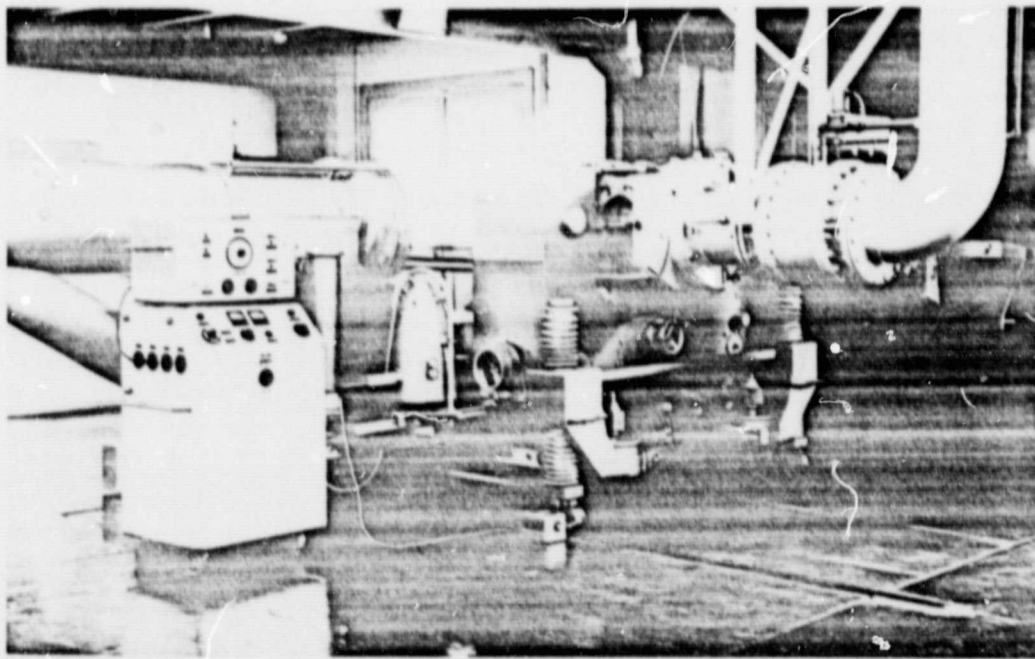Figure 7: Opened Tunnel, without Accessories and
without inlet jet
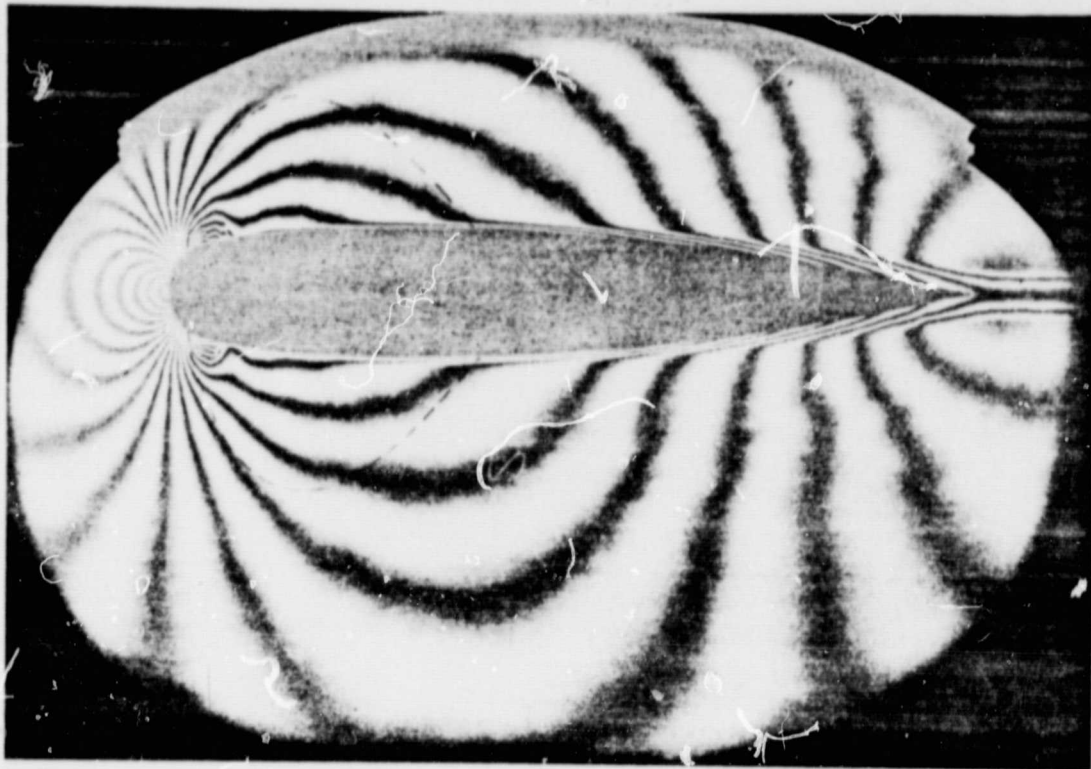

Figure 8: Complete Picture of the Test Arrangement

Fig. 9: Interferogram of the Flow for $M_{oo} = 0.690$
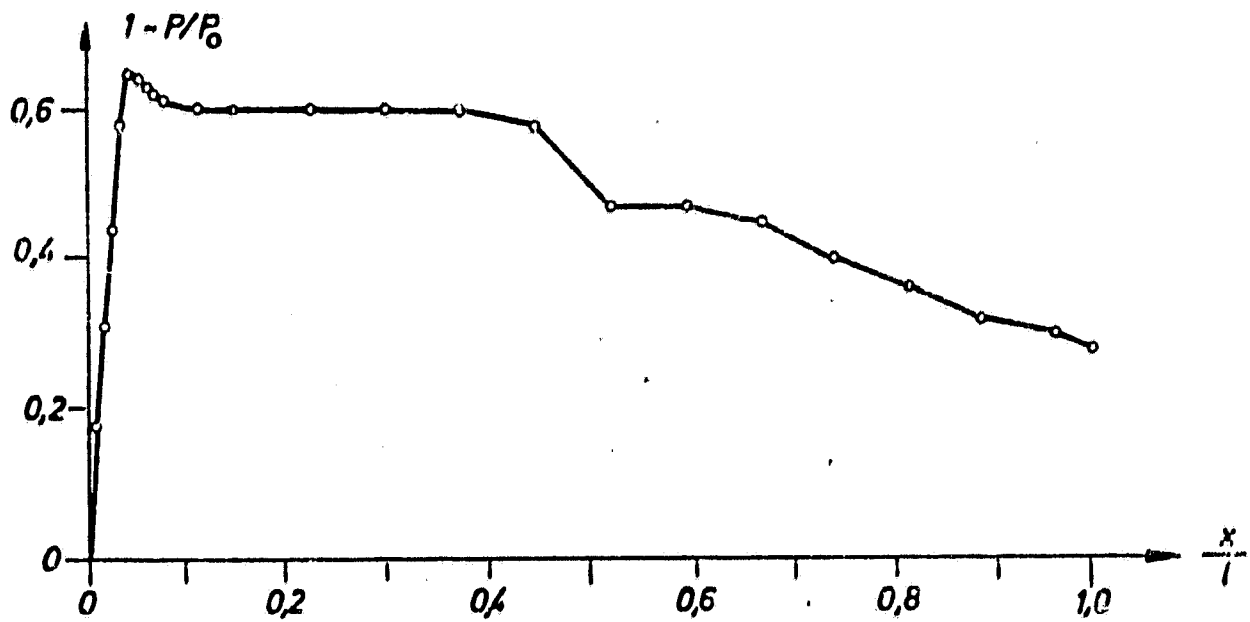--- = calculated sonic barrier for $M_{oo} = 0.745$
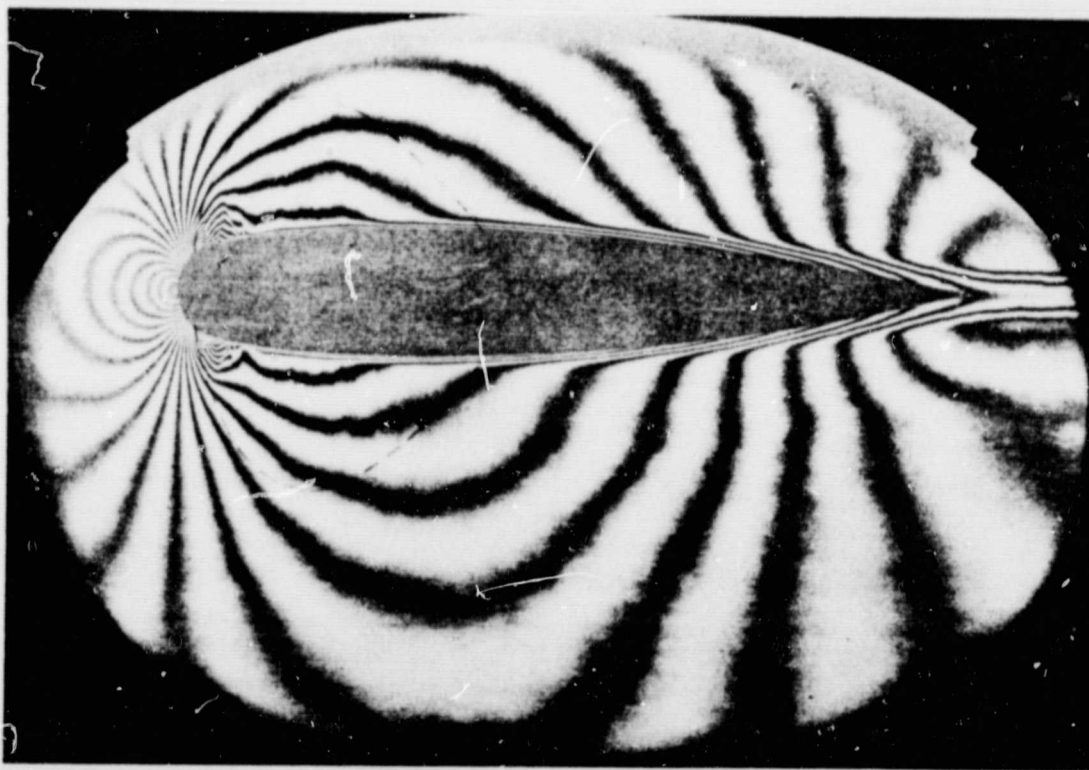
Fig. 10: $M_{oo} = 0.73$
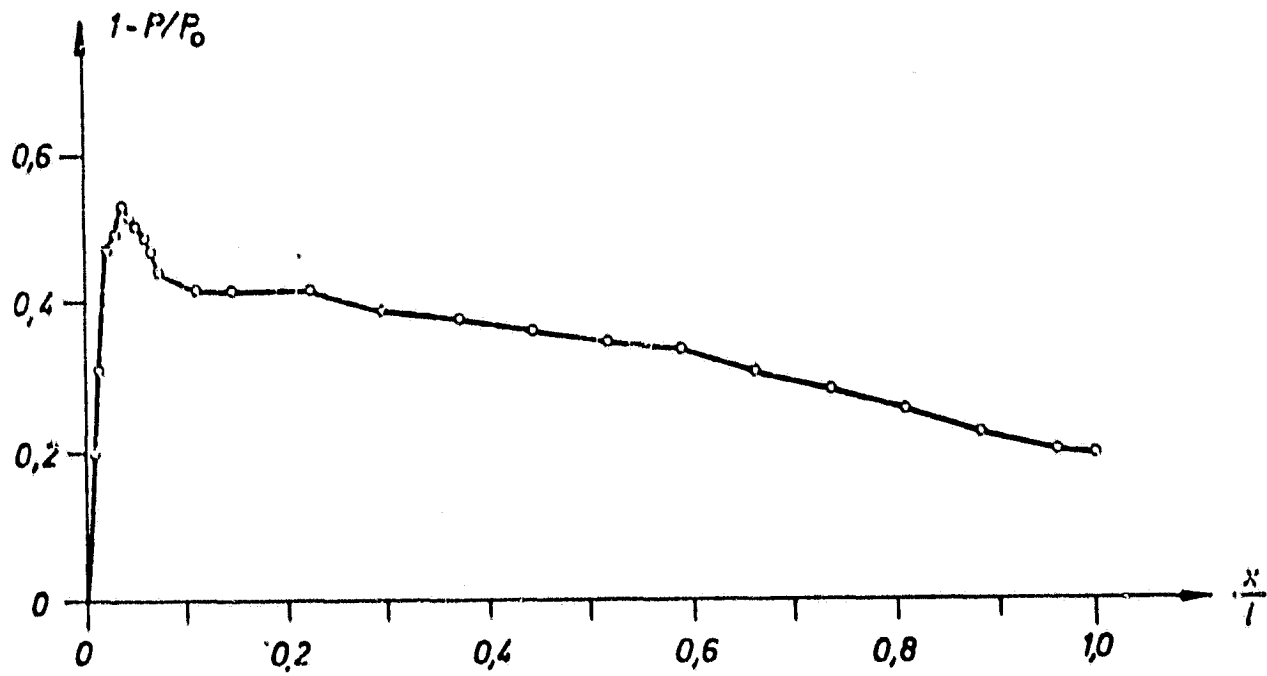
Fig. 9a: Pressure Distribution on the Profile top Side.
1 length of chord of the profile
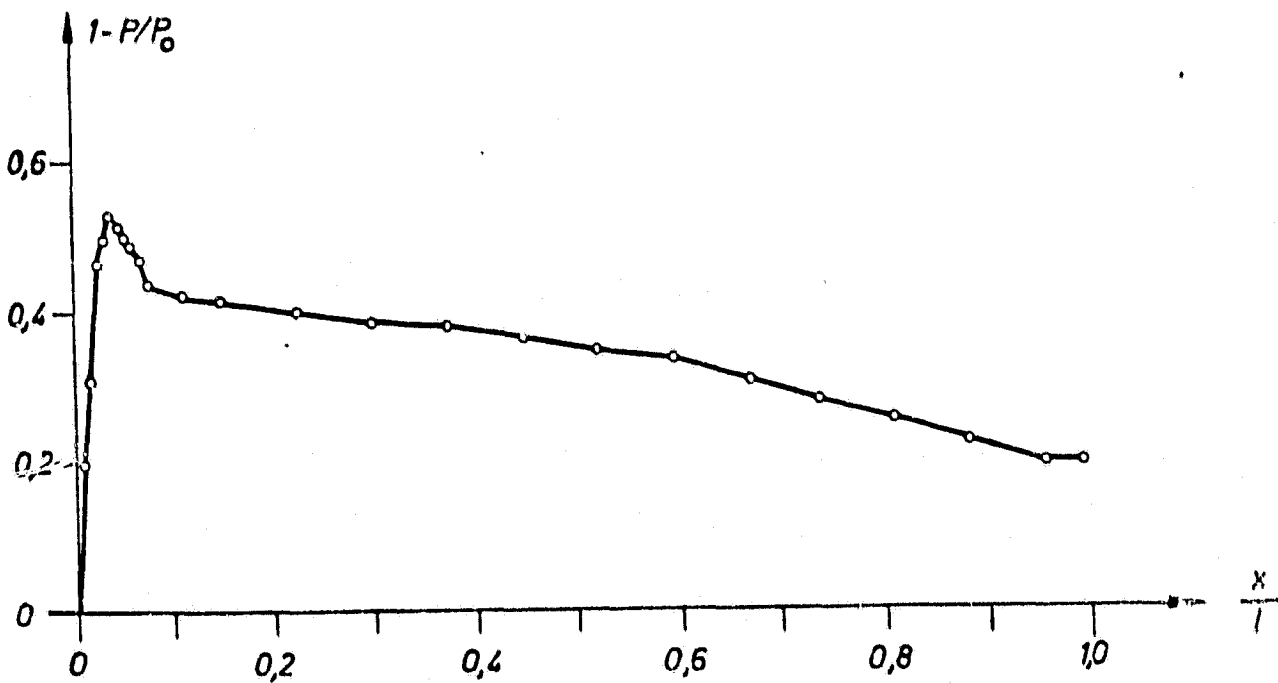
Fig. 9b: Pressure Distribution on the Profile lower Side
1 length of chord of the profile

14
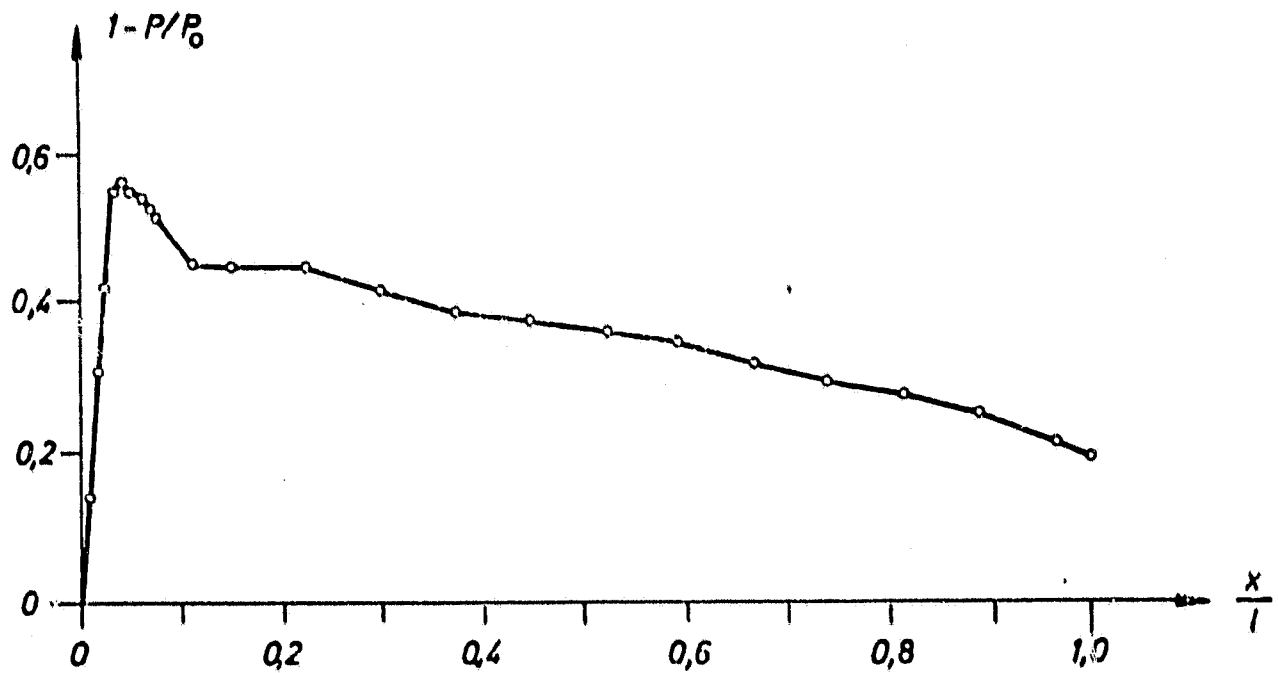
Fig. 10a: Pressure Distribution on the Profile top Side
1 length of chord of the profile
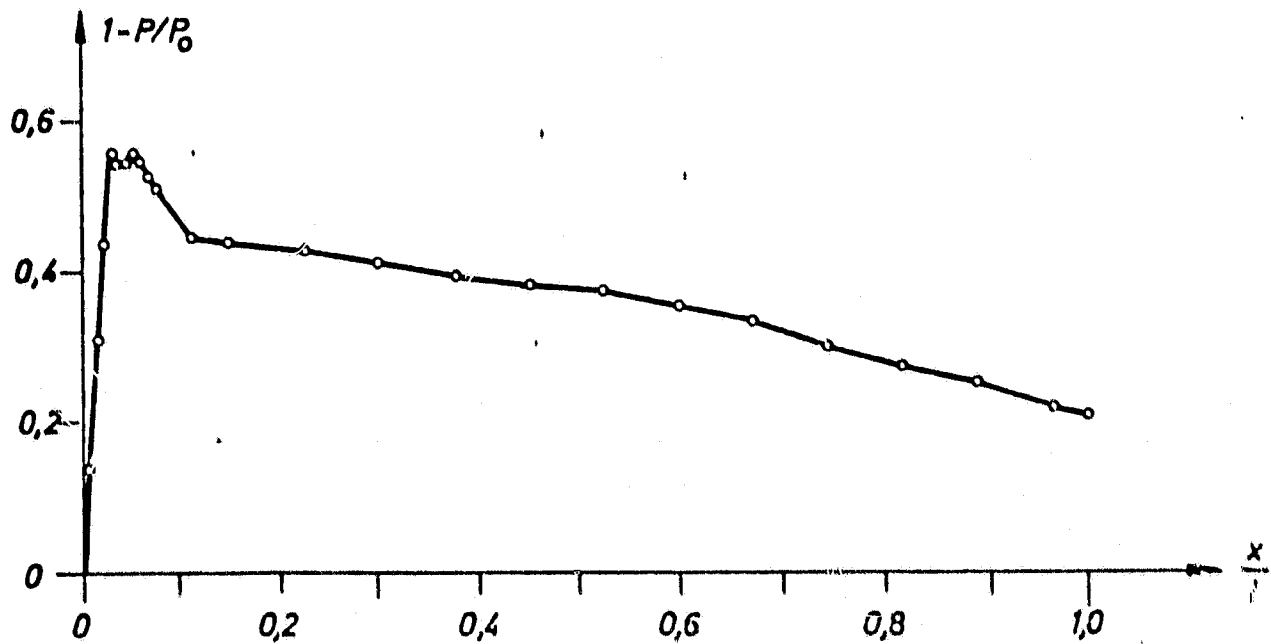
Fig. 10b: Pressure Distribution on the Profile lower Side
1 length of chord of the profile
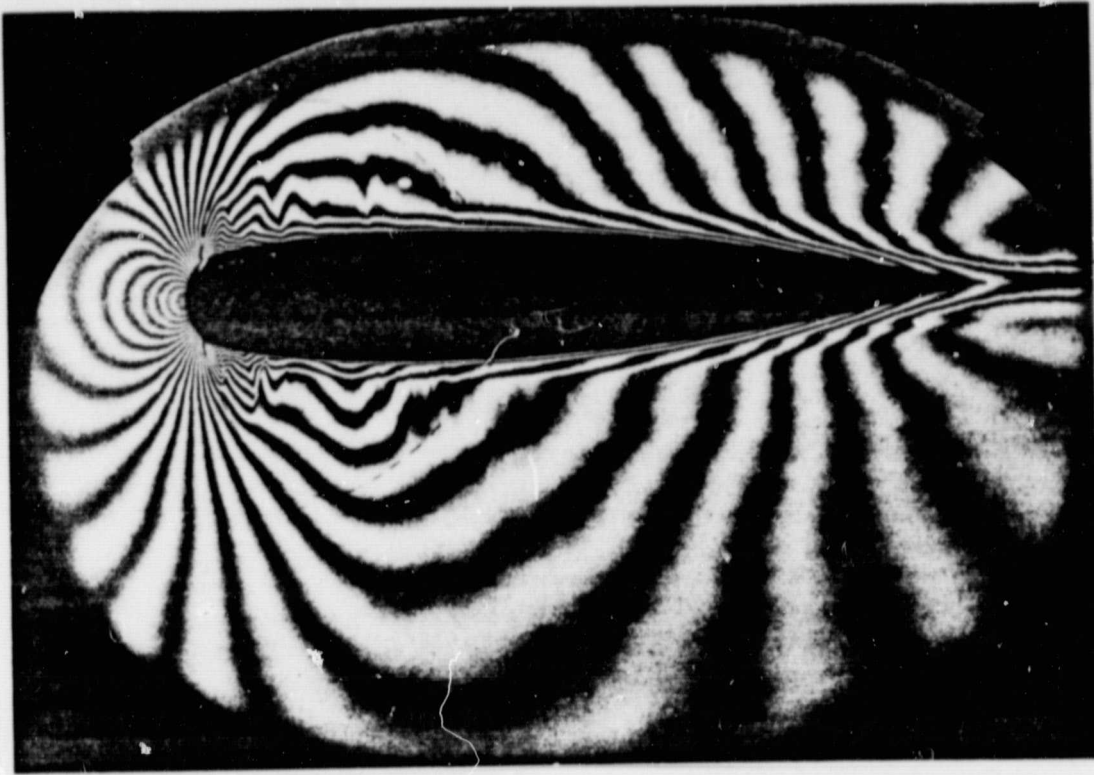
Figure 11: $M_{\infty} = 0.78$
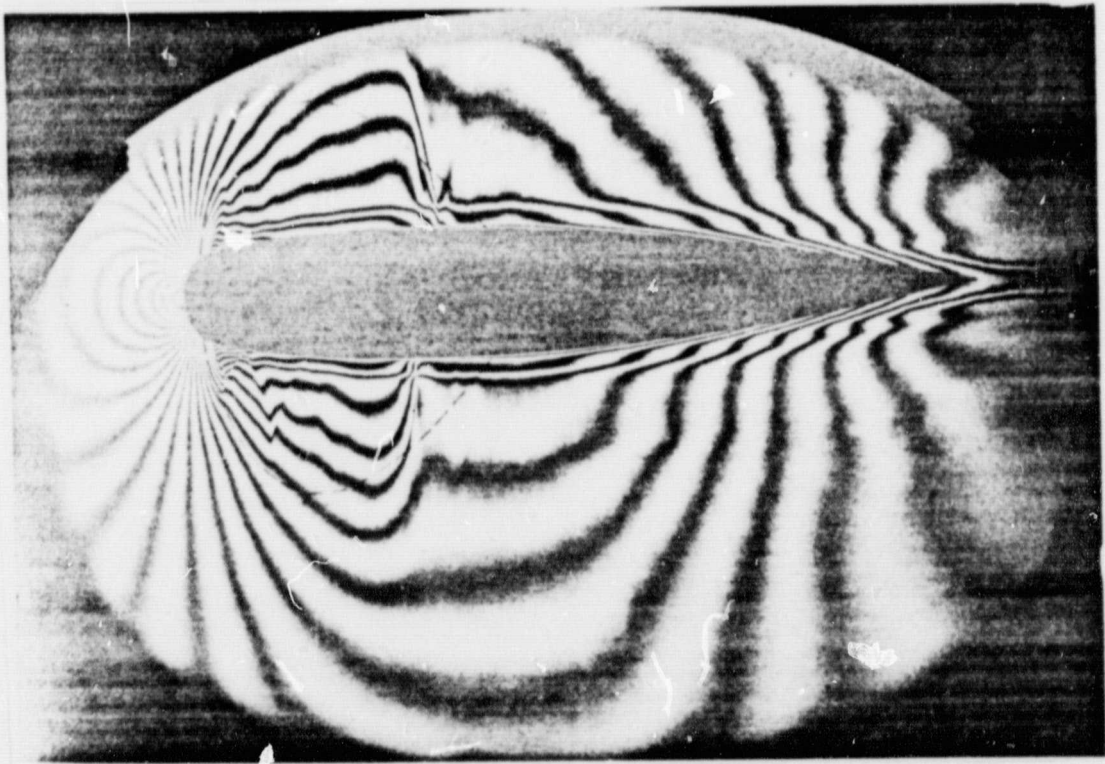
Figure 12: $M_{\infty} = 0.796$

16
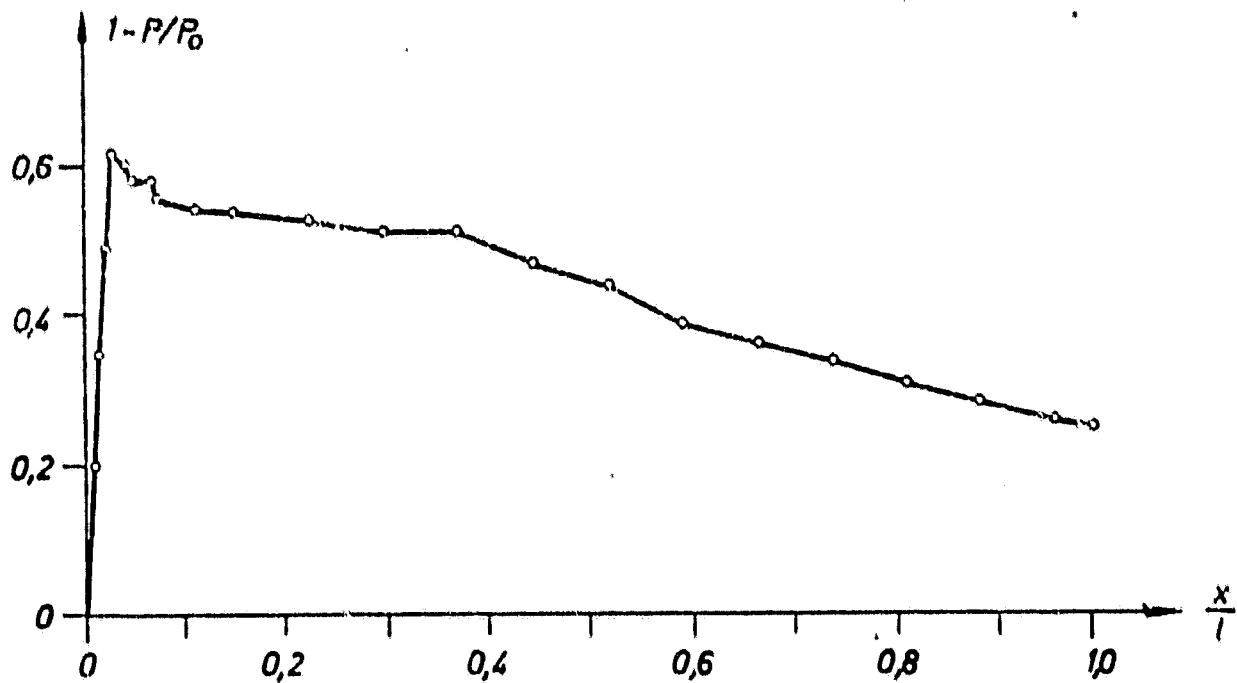
Fig. 11a: Pressure Distribution on the Profile top Side
1 length of chord of the profile
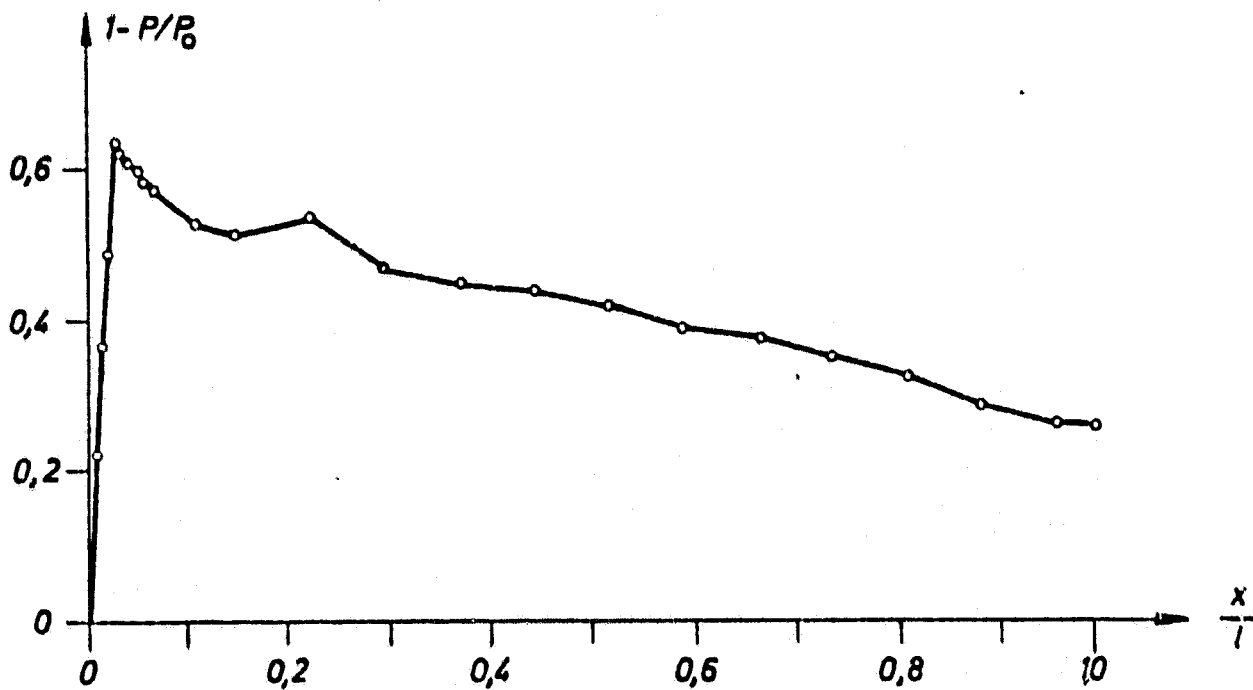
Fig. 11b: Pressure Distribution on the Profile lower Side
1 length of chord of the profile
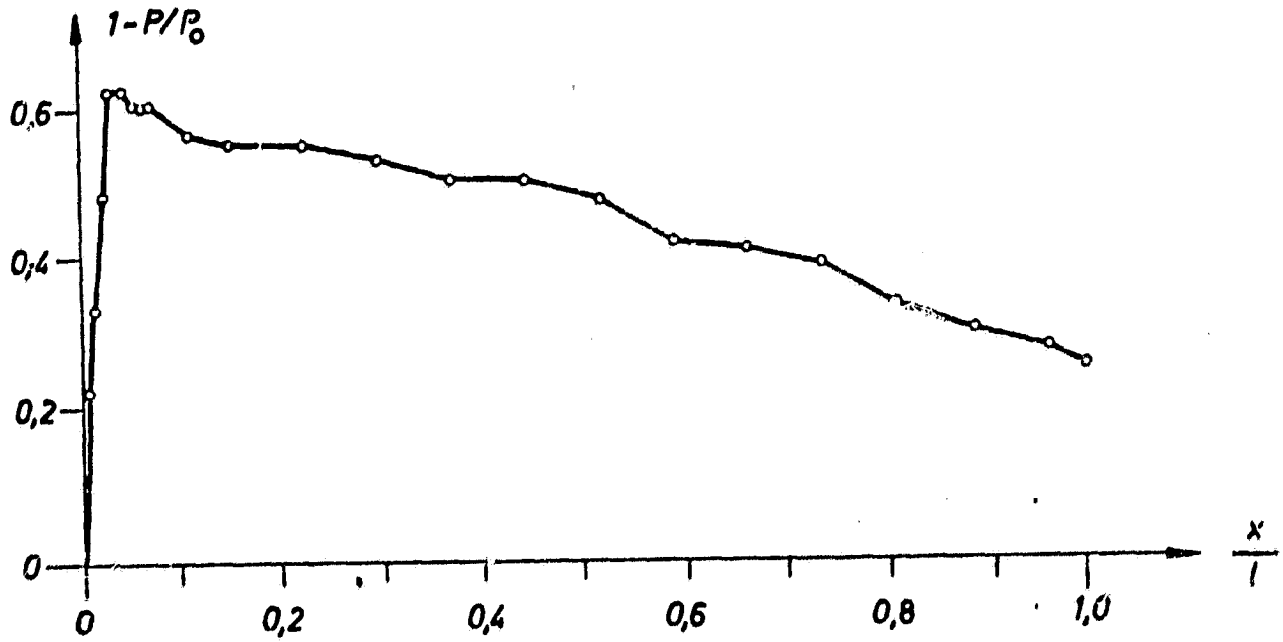
Fig. 12a: Pressure Distribution on the profile top Side
1 length of chord of the profile
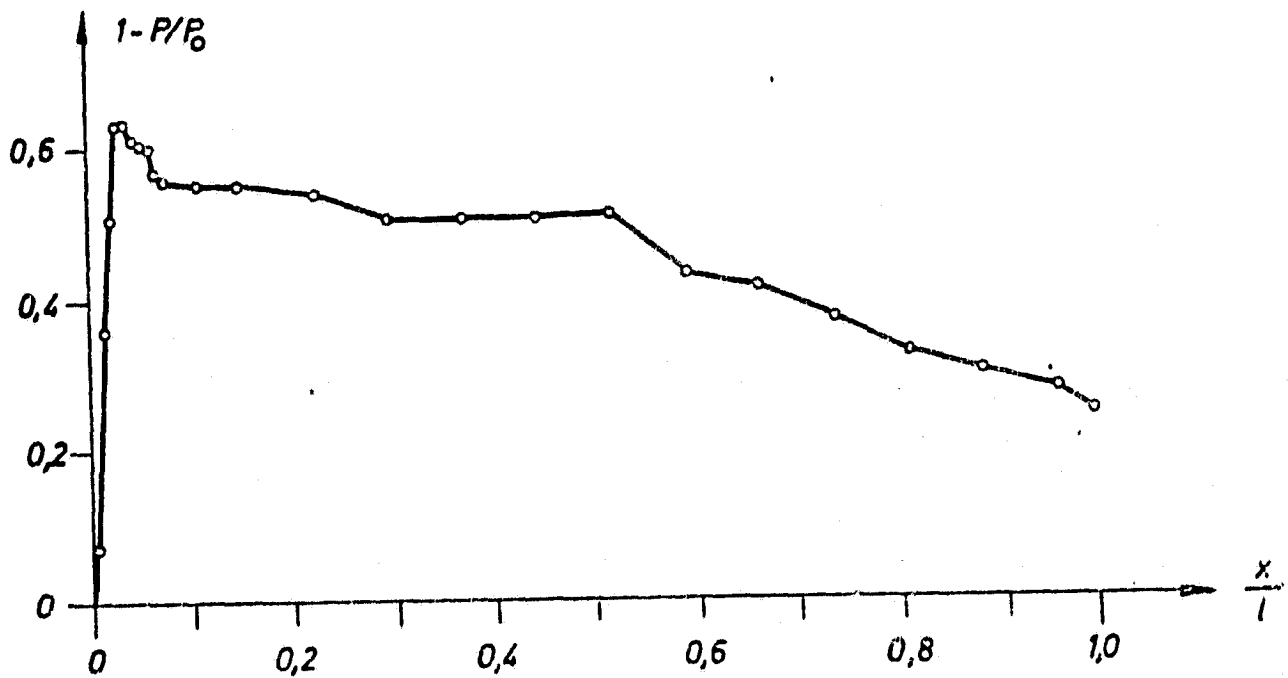
Fig. 12b: Pressure Distribution on the Profile lower Side
1 length of chord of the profile
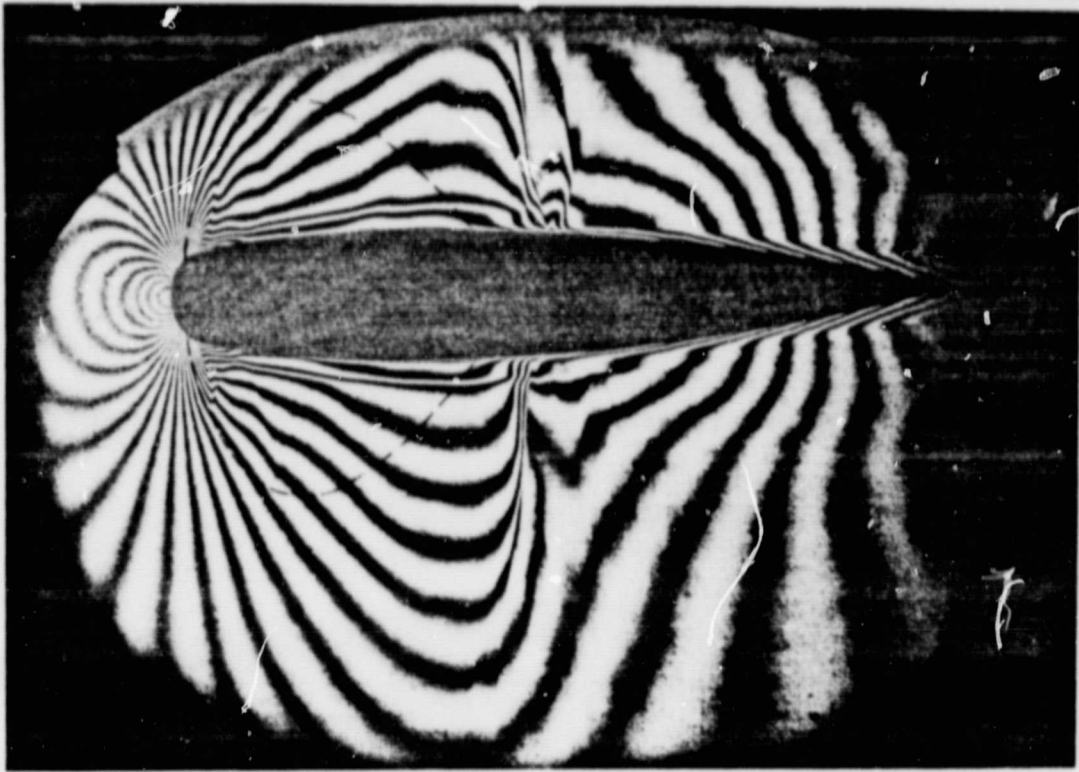
Figure 13: $M_{oo} = 0.80$
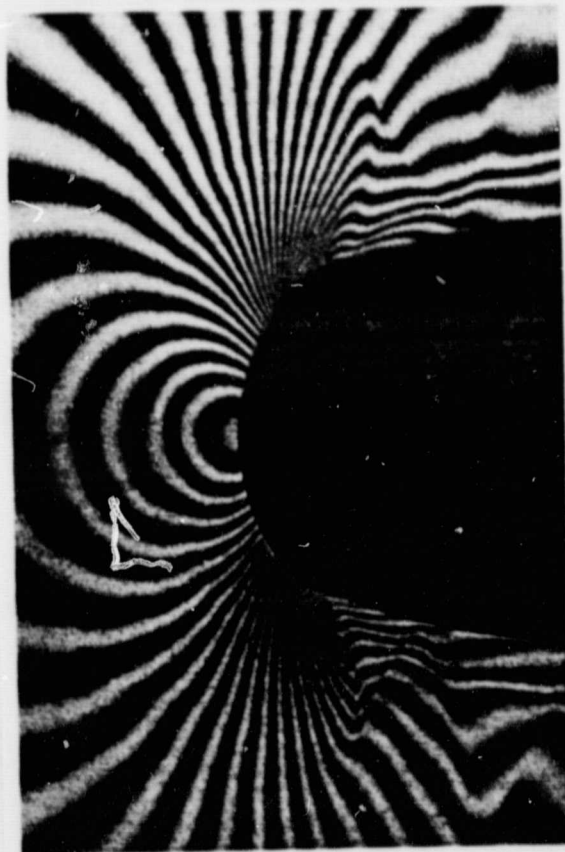
Fig. 14: Flow in the environ of the profile nose

19

Fig. 13a: Pressure Distribution on the Profile top Side
1 length of chord of the profile
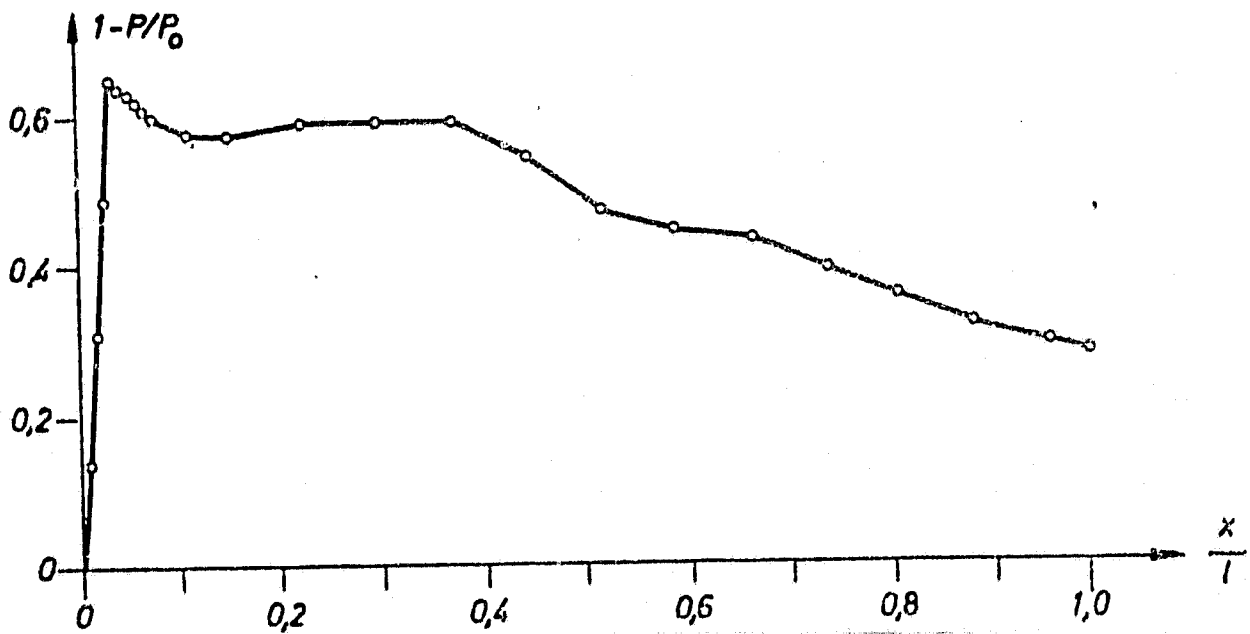
Fig. 13b: Pressure Distribution on the Profile lower Side
1 length of chord of the profile
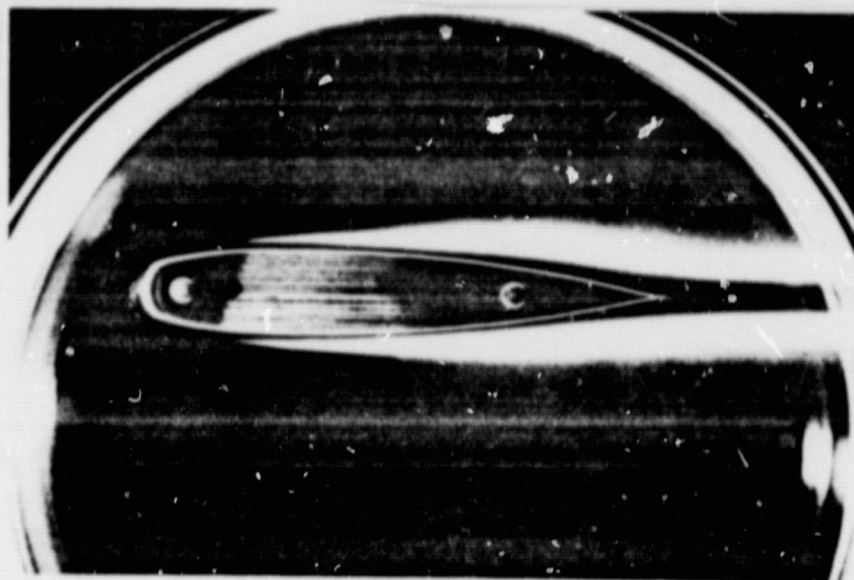
Figure 15: Water Vapor Condensation, $M_{oo} = 0.78$
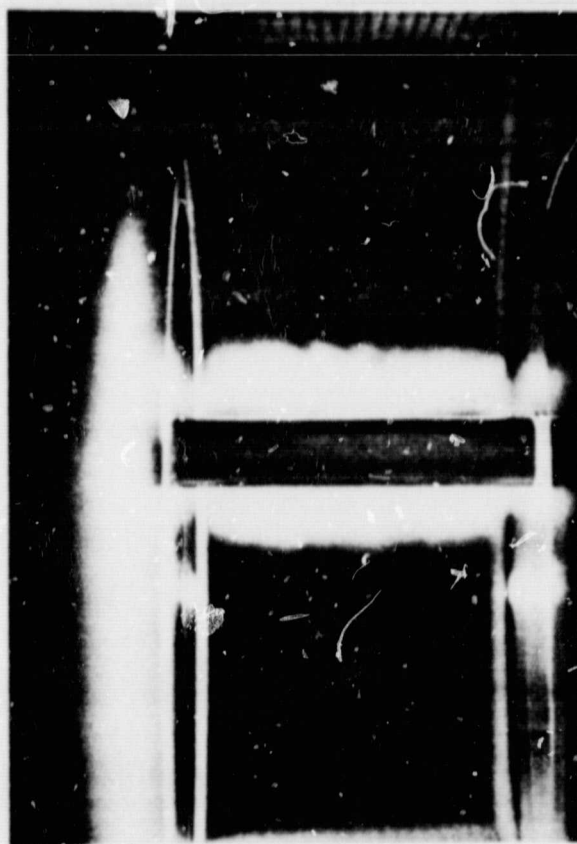
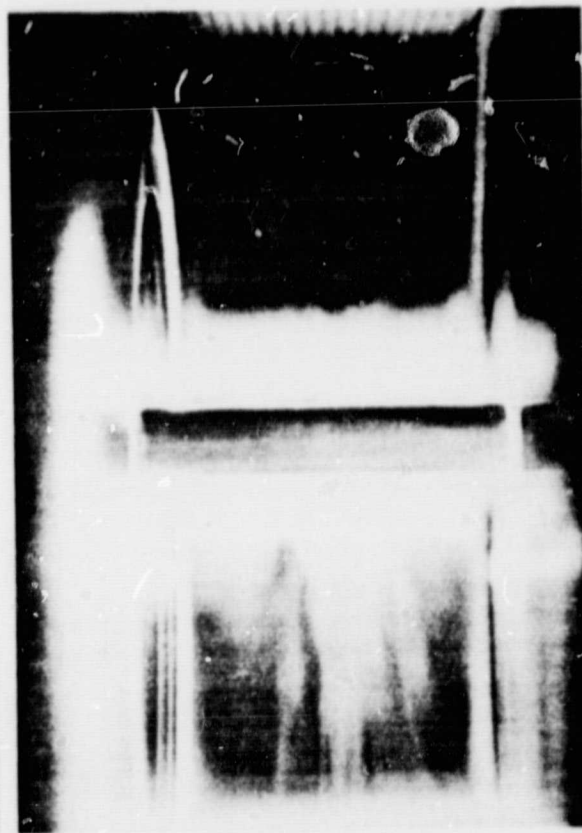Figure 16: Water Vapor Condensation, $M_{oo} = 0.78$
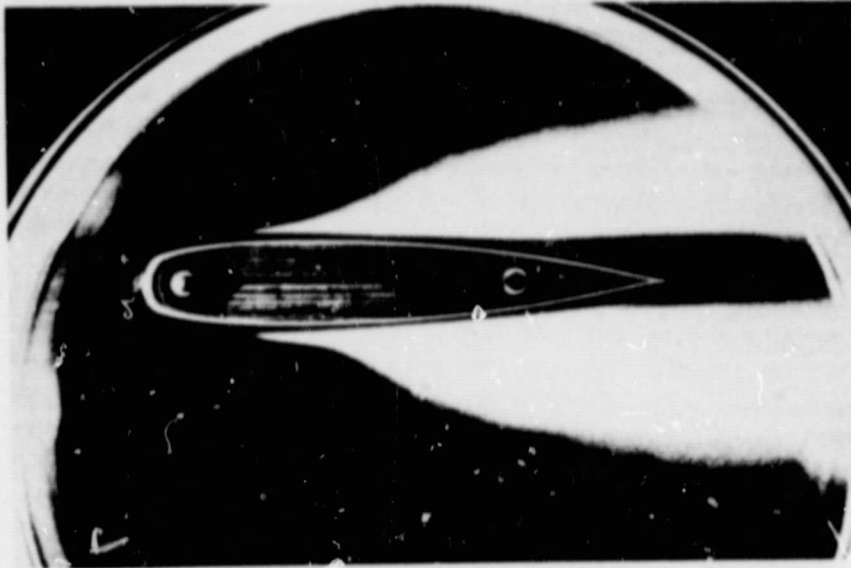
Figure 17: Water Vapor condensation, $M_{oo} = 0.80$

Figure 18: Water Vapor Condensation, $M_{oo} = 0.80$

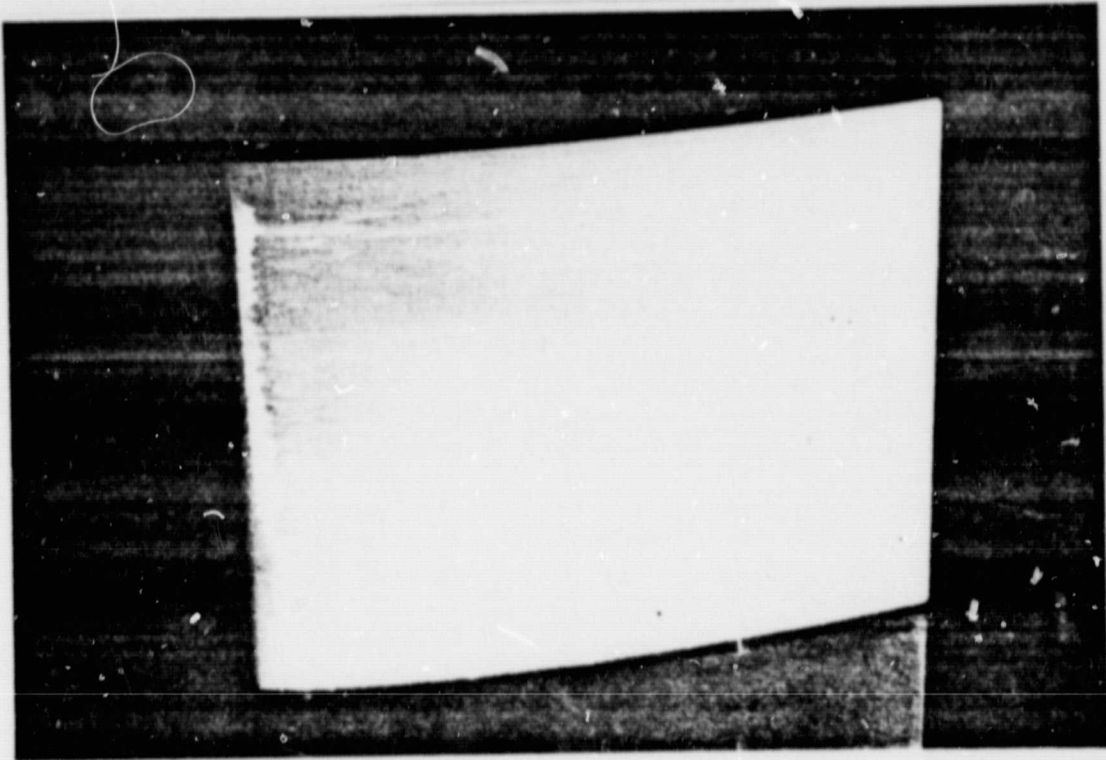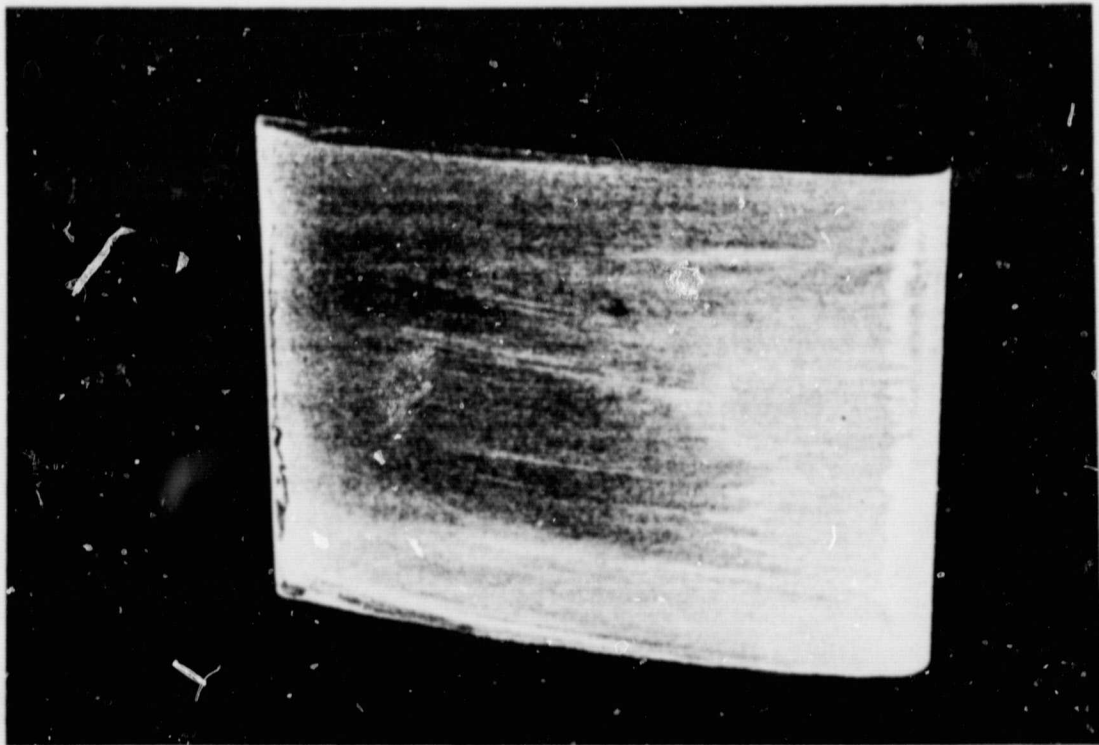Detection of Boundary Layer separation by the tinting method

Figure 19: Top Side of the Profile

Figure 20: Lower Side of the Profile